K. Somesh, Y. Furukawa, G. Simutis, F. Bert, M. Prinz-Zwick, N. Büttgen, A. Zorko, A. A. Tsirlin, P. Mendels, and R. Nath

# Universal fluctuating regime in triangular chromate antiferromagnets

K. Somesh,[1] Y. Furukawa,[2] G. Simutis,[3] F. Bert,[3] M. Prinz-Zwick,[4] N. Büttgen,[4] A. Zorko,[5, 6] A. A. Tsirlin,[7, *] P. Mendels,[3, †] and R. Nath[1, ‡]

[1] *School of Physics, Indian Institute of Science Education and Research Thiruvananthapuram-695551, India*
[2] *Ames Laboratory and Department of Physics and Astronomy, Iowa State University, Ames, Iowa 50011, USA*
[3] *Université Paris-Saclay, CNRS, Laboratoire de Physique des Solides, 91405, Orsay, France*
[4] *Experimental Physics V, Center for Electronic Correlations and Magnetism,*
*University of Augsburg, D-86159 Augsburg, Germany*
[5] *Jožef Stefan Institute, Jamova c. 39, SI-1000 Ljubljana, Slovenia*
[6] *Faculty of Mathematics and Physics, University of Ljubljana, SI-1000 Ljubljana, Slovenia*
[7] *Experimental Physics VI, Center for Electronic Correlations and Magnetism,*
*University of Augsburg, 86135 Augsburg, Germany*
(Dated: September 10, 2021)

We report x-ray diffraction, magnetic susceptibility, heat capacity, $^1$H nuclear magnetic resonance (NMR), and muon spin relaxation ($\mu$SR) measurements, as well as density-functional band-structure calculations for the frustrated $S = 3/2$ triangular lattice Heisenberg antiferromagnet (TLHAF) $\alpha$-HCrO$_2$ (trigonal, space group: $R\bar{3}m$). This compound undergoes a clear magnetic transition at $T_N \simeq 22.5$ K, as seen from the drop in the muon paramagnetic fraction and concurrent anomalies in the magnetic susceptibility and specific heat capacity. Local probes (NMR and $\mu$SR) reveal a broad regime with slow fluctuations down to $0.7\,T_N$, this temperature corresponding to the maximum in the $\mu$SR relaxation rate and in the NMR wipe-out. From the comparison with NaCrO$_2$ and $\alpha$-KCrO$_2$, the fluctuating regime and slow dynamics below $T_N$ appear to be hallmarks of the TLHAF with $ABC$ stacking. We discuss the role of interlayer frustration which may bear implications to recent spin-liquid candidates with the triangular geometry.

## I. INTRODUCTION

Experimental realization of quantum spin liquid (QSL) remains one of the major challenges in condensed-matter physics [1, 2]. An identification of this exotic entangled state in real-world materials could open the way to understanding and utilizing fractionalized excitations, which are particularly interesting in the context of quantum computing [3]. Theoretical studies established several promising settings for the QSL that were indeed proposed [4] in antiferromagnets with the kagome [5], triangular [6], and honeycomb [7] structures, all of them based on the two-dimensional interaction geometries.

Recent work on triangular antiferromagnets [6] exposed the $A$Yb$X_2$ compound family ($A$ = Na, K and $X$ = O, S, Se) as the largest stock of the QSL candidates known to date. In fact, all members of this family evade long-range magnetic order [8–13], while some of them additionally show spectral signatures of fractionalized spinon excitations [14] or excitations of a Dirac QSL [15, 16]. One potentially important but hitherto neglected feature of these compounds is the $ABC$-type stacking of their triangular layers that causes frustration of the interlayer couplings, as shown in Fig. 1. Each magnetic site is coupled to three sites of the adjacent layer. This arrangement prevents simple ferro- or antiferromagnetic order along $c$.

Here, we explore the effect of this intra and inter-layer frustration using the $A$CrO$_2$ chromates. These compounds are convenient model systems that contain semi-classical spins $\frac{3}{2}$ and, thanks to the half-filled $t_{2g}$ shell of Cr$^{3+}$, feature isotropic Heisenberg interactions within the triangular planes. Such an interaction regime is known to induce 120° order in the plane, which is indeed observed in LiCrO$_2$ [17–20], but other members of the same family do not show a clear magnetic ordering. In NaCrO$_2$, a transition at $T_N \simeq 41$ K is followed by a broad fluctuating regime with slow dynamics extending down to $T^* \simeq 30$ K [21] for which the occurrence of Berezinskii-Kosterlitz-Thouless (BKT) was suggested [22]. On the other hand, $\alpha$-HCrO$_2$ with the shortest interlayer distance was recently claimed to evade magnetic order and lie in the vicinity of a spin-liquid phase [23]. Using a combination of thermodynamic and local probes applied to $\alpha$-HCrO$_2$, we show that in fact all these chromates – NaCrO$_2$, $\alpha$-HCrO$_2$, as well as $\alpha$-KCrO$_2$ [24] – develop a very similar phenomenology. They enter a broad universal fluctuating regime below $T_N$, followed by the formation of a static and likely incommensurate spin state below $T^*$. Our findings reveal a new mechanism of creating fluctuating spin-liquid-like states that reside on the triangular planes but crucially rely on the interlayer frustration.

## II. METHODS

A polycrystalline sample of $\alpha$-HCrO$_2$ was prepared by an hydrothermal method. It involves two steps. First,
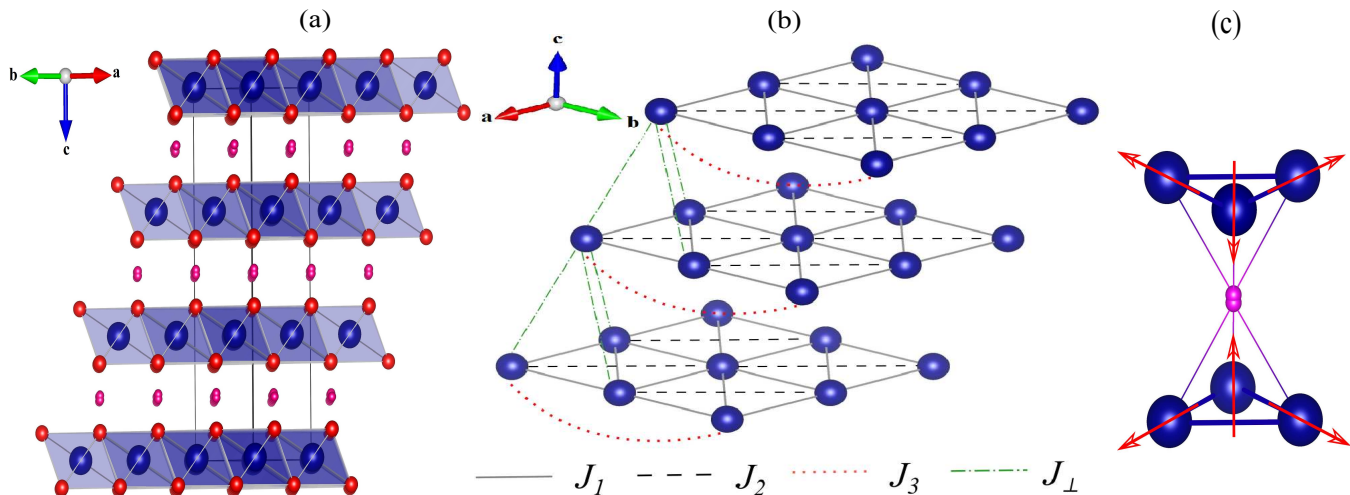
FIG. 1. (a) Crystal structure of $\alpha$-HCrO$_2$ consisting of triangular layers formed by CrO$_6$ octahedra and H atoms at the interstitial sites. (b) Triangular Cr layers showing possible exchange couplings $J_1$, $J_2$, $J_3$, and $J_\perp$ between the Cr$^{3+}$ ions. (c) Coupling of H with three Cr$^{3+}$ ions from each layer where spins are arranged in a $120°$ structure.

the intermediate oxide Cr$_8$O$_{21}$ was prepared by heating CrO$_3$ (Aldrich, 99.99% pure) granules for 12 hours at 250 °C in air. In the second step, the intermediate product was crushed into fine powder, put into a 1 M LiOH solution in deionized water, heated at 200 °C in a teflon-lined stainless steel autoclave for about one week, and subsequently furnace-cooled. The phase purity of the product was confirmed by powder x-ray diffraction (XRD) using a PANalytical x-ray diffractometer (Cu $K_\alpha$ radiation, $\lambda_{av} = 1.54182$ Å). The temperature-dependent powder XRD measurement was performed over the temperature range 15 K$\leq T \leq 300$ K using the low-temperature attachment (Oxford Phenix) to the diffractometer.

Magnetization ($M$) measurements were performed as a function of temperature ($T$) and applied field ($H$) using a superconducting quantum interference device (MPMS-3, Quantum Design). Heat capacity [$C_p(T)$] as a function of $T$ and $H$ was measured on a small piece of sintered pellet using the relaxation technique in the physical property measurement system (PPMS, Quantum Design).

The NMR measurements were carried out using pulsed NMR techniques on $^1$H (nuclear spin $I = 1/2$ and gyromagnetic ratio $\gamma_N/2\pi = 42.575$ MHz/T) nuclei in the temperature range 1.6 K $\leq T \leq 250$ K and at different radio frequencies. The spectra were obtained either by Fourier transform (FT) of the NMR echo signal or by sweeping the magnetic field. The NMR shift $K = (\nu - \nu_{\rm ref})/\nu_{\rm ref}$ was determined by measuring the resonance frequency of the sample ($\nu$) with respect to nonmagnetic reference H$_2$O (resonance frequency $\nu_{\rm ref}$). The $^1$H spin-lattice relaxation rate ($1/T_1$) was measured by the conventional inversion recovery method. The spin-spin relaxation rate ($1/T_2$) was measured through the decay of the echo integral with variable spacing between the $\pi/2$ and $\pi$ pulses.

The muon spin rotation/relaxation ($\mu$SR) experiments were carried out at the $\pi$M$_3$ beam line using the GPS spectrometer at the Paul Scherrer Institute (PSI), Switzerland [25]. The zero-field (ZF) and the weak transverse-field (wTF) $\mu$SR measurements were performed at temperatures ranging from $\sim$ 1.5 K to 50 K. The 100% spin-polarized $\mu^+$ (spin-1/2 and gyromagnetic ratio $\gamma_\mu = 135.5$ MHz/T) with the momentum of $\sim$ 28.6 MeV/c were implanted into the sample. Because of their positive charge, muons come at rest in well-defined sites where their electrostatic energy is minimized, i.e. in oxides typically 1 Å away from an oxygen O$^{2-}$ site. They usually interact with surrounding moments through a dipolar coupling. In a paramagnetic state, the electronic moments fluctuate fast ($\sim 10^{-12}$ s) on the $\mu$SR time scale and the static field sensed by the muons has only a nuclear origin with a typical value of a few Gauss, while dynamical electronic fields lead to motional narrowing. On the contrary, when electronic moments slow down, the evolution of the ZF polarization with time witnesses both their dynamics and freezing. At the base temperature ($T \ll T_N$), very high counting statistics ($\sim$ 115 Mevents) were taken in order to track the fast-decaying polarization measured in zero-field, where the contribution from static electronic moments dominates.

Density-functional (DFT) band-structure calculations were performed in the FPLO code [26] using the Perdew-Burke-Ernzerhof flavor of the exchange-correlation potential [27]. Correlation effects in the Cr $3d$ shell were taken into account of the mean-field DFT+$U$ level using the on-site Coulomb repulsion $U_d = 2$ eV, Hund's coupling $J_d = 1$ eV, and atomic limit for the double-counting correction [28, 29]. Experimental structural parameters for LiCrO$_2$ [30], NaCrO$_2$ [31], and $\alpha$-KCrO$_2$ [31] have been used. In the case of $\alpha$-HCrO$_2$, the position of hy-

drogen remains somewhat uncertain. We thus considered two limiting cases: i) hydrogen placed in the middle between the $CrO_2$ layers, with the $R\bar{3}m$ symmetry preserved; ii) hydrogen displaced toward one of the layers. In the latter case, the symmetry is reduced to $R3m$, and the individual $CrO_6$ octahedra are slightly distorted, because the Cr–O distances can be shorter or longer depending on how strongly the oxygen atom binds to the hydrogen. Room-temperature atomic positions from Ref. [32] have been used, as they feature the largest distortion and allow one to test its effect on magnetism. Exchange parameters $J_{ij}$ and single-ion anisotropy $D$ enter the spin Hamiltonian,

$$\mathcal{H} = \sum_{\langle ij \rangle} J_{ij} \mathbf{S}_i \mathbf{S}_j - \sum_i D(S_i^z)^2, \qquad (1)$$

where the summation is over atomic pairs $\langle ij \rangle$, and $S = \frac{3}{2}$. The parameters of this Hamiltonian were obtained by a mapping procedure [33] from total energies of magnetically ordered states.

### III. RESULTS

#### A. X-ray Diffraction

In order to confirm the phase purity and to check the presence of any structural distortions, powder XRD data were collected at various temperatures. The Rietveld refinements of the XRD patterns were executed using the `FullProf` software package [34] with the initial parameters taken from Ref. [32]. Figure 2 presents the powder XRD patterns at 300 and 15 K along with the Rietveld fits. At room temperature, all the peaks could be indexed based on the space group $R\bar{3}m$ (No. 166) suggesting phase purity of the sample. A small difference between the experimental and calculated intensities at $2\theta \sim 38°$ is likely due to preferred orientation effects expected in a layered compound. The obtained lattice parameters at room temperature are $a = b = 2.9836(1)$ Å, $c = 13.4232(1)$ Å, and unit cell volume $V_{cell} \simeq 103.48$ Å$^3$, which are comparable with the previous report [32]. No extra features or peaks were observed in the XRD scans implying the absence of any structural transitions down to 15 K. On the other hand, around 30 K both lattice parameters ($a$ and $c$) clearly deviate from their anticipated low-temperature behavior [see Fig. 2(c)]. Such weak kinks, humps, and changes of slope are commonly observed in magnetic compounds in the vicinity of their magnetic transitions, where lattice symmetry does not change but a magnetoelastic coupling leads to anomalies in thermal expansion [35, 36].

The temperature variation of the lattice constants ($a$ and $c$) and unit cell volume ($V_{cell}$) as shown in Fig. 2(c) are found to decrease monotonically upon cooling down to $T \approx 45$ K. $V_{cell}(T)$ above 45 K was fitted by the equa-
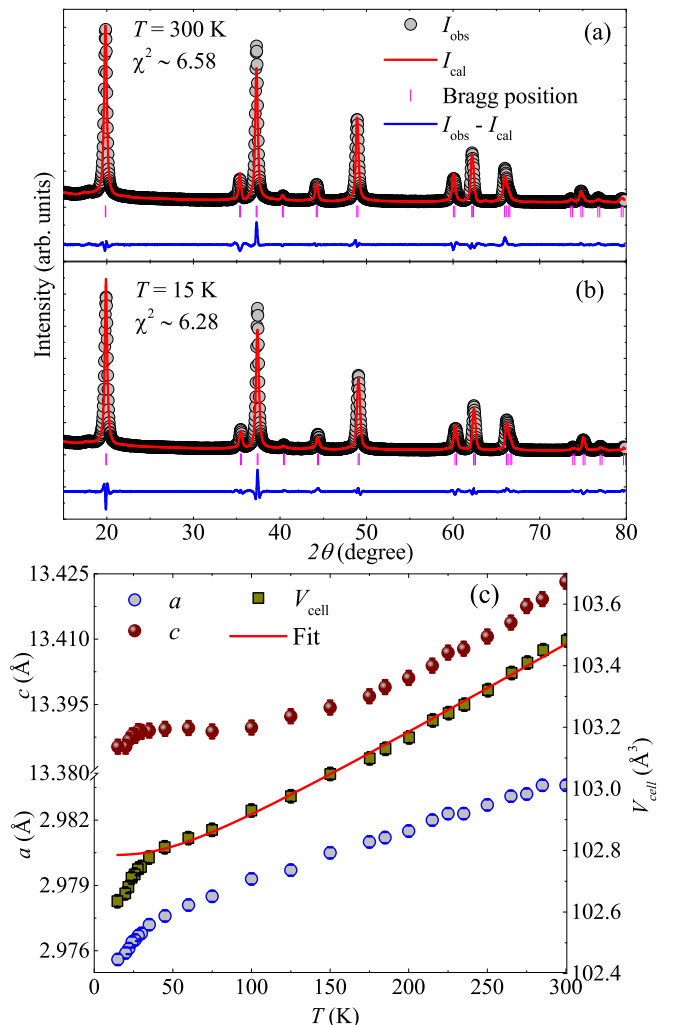


FIG. 2. Powder XRD data measured at (a) $T = 300$ and (b) $T = 15$ K. The red solid line represents the Rietveld fit of the data. The Bragg positions are indicated by pink vertical bars and the solid blue line at the bottom denotes the difference between the experimental and calculated intensities. (c) The variation of the lattice parameters ($a$, $c$, and $V_{cell}$) as a function of temperature. The solid line denotes the fit of the $V_{cell}(T)$ by Eq. (2).

tion [37]

$$V(T) = \gamma U(T)/K_0 + V_0, \qquad (2)$$

where $V_0$ is the cell volume in the zero temperature limit, $K_0$ is the bulk modulus, and $\gamma$ is the Grüneisen parameter. $U(T)$ is the internal energy, which can be derived in terms of the Debye approximation as

$$U(T) = 9nk_BT \left( \frac{T}{\theta_D} \right)^3 \int_0^{\theta_D/T} \frac{x^3}{e^x - 1} dx. \qquad (3)$$

Here, $n$ is the number of atoms in the unit cell and $k_B$ is the Boltzmann constant. Using this approximation [see Fig. 2(c)], the Debye temperature ($\theta_D$) and other
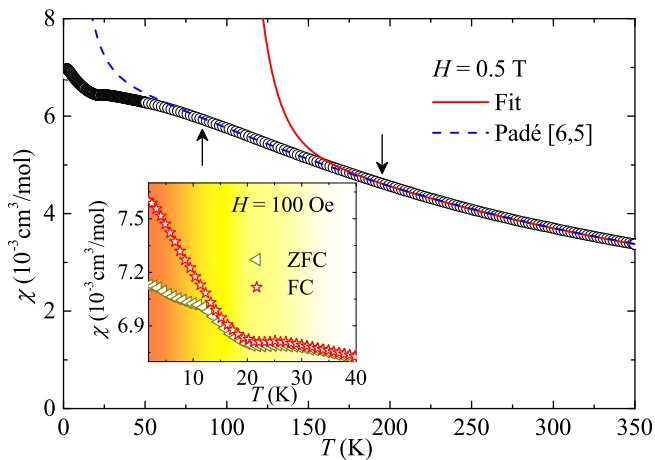
FIG. 3. Temperature dependence of magnetic susceptibility [$\chi(T)$] measured in an applied field of 0.5 T and in the temperature range 1.8 K≤ $T$ ≤ 350 K. The solid and dashed lines denote the fits by Eq. (4) and Padé approximation, respectively. Arrows signal the limit of validity of HTSE or Padé approximation. Inset: Zero-field-cooled (ZFC) and field-cooled (FC) magnetic susceptibilities as a function of temperature measured in an field of 100 Oe.

parameters were estimated to be $\theta_D = 195(9)$ K, $\gamma/K_0 = 2.95(7) \times 10^{-5}$ Pa$^{-1}$, and $V_0 \simeq 102.8(7)$ Å$^3$.

## B. Magnetization

Previous magnetic susceptibility $\chi(T)$ and $^1$H NMR measurements were restricted to temperatures above the possible magnetic ordering [38, 39]. An antiferromagnetic transition at $T_N \sim 25$ K has been reported from the heat capacity measurements [40].

The temperature-dependent magnetic susceptibility $\chi(T)$ ($\equiv M/H$) measured in an applied field of 0.5 T is shown in Fig. 3. As expected in the paramagnetic regime, $\chi(T)$ increases with decreasing temperature in a Curie-Weiss manner but becomes flatter toward lower temperatures when spin-spin correlations set in. A hump around 27 K coincides with the lattice anomaly discussed above. At even lower temperatures, $\chi(T)$ shows an upturn around 20 K and a splitting at 12 K between field-cooled (FC) and zero-field-cooled (ZFC) curves measured in a weak applied field. While the latter signature may be indicative of spin freezing, our frequency-dependent AC susceptibility measurement (see, Supplementary Materials [41]) rules out the possibility of a conventional spin-glass transition.

Traditionally, $\chi(T)$ is fitted by the sum of a temperature independent term ($\chi_0$) and of a Curie-Weiss law, $\chi_0 + \frac{C}{T-\theta_{CW}}$ in order to obtain the Curie constant $C$ and the characteristic CW temperature $\theta_{CW}$. $C$ yields the effective moment while $\theta_{CW}$ represents the energy scale of the total exchange interactions. $\theta_{CW}$ is given by: $|\theta_{CW}| = \frac{JzS(S+1)}{3k_B}$, where $z = 6$ is the number of nearest-

neighbours of Cr$^{3+}$ ions and $J$ ($= J_1$) is the intra-layer exchange coupling [42]. This requires the $T$ range of the measurements to fall into the high-temperature regime, $T \gg |\theta_{CW}|$ which is not the case here. Indeed, our $\chi(T)$ data are limited up to 350 K and $\theta_{CW}$ for HCrO$_2$ is in the range $220 - 270$ K [38].

We therefore used high-temperature series expansion (HTSE), now available up to 11$^{th}$ order [43] and Padé approximants [44] to fit our data,

$$\chi = \chi_0 + \chi_{spin}(T) \quad (4)$$

and

$$\chi_{spin}(T) = \frac{N_A g^2 \mu_B^2}{k_B T} \times \left[ \frac{5}{4} - \frac{75}{8}x + \frac{225}{4}x^2 \right.$$
$$- \frac{18765}{64}x^3 + \frac{712175}{512}x^4 - \frac{6328661}{1024}x^5 + \frac{643219519}{24576}x^6$$
$$- \frac{36677316665}{344064}x^7 + \frac{1154751891527}{27525127}x^8$$
$$\left. - \frac{1888217340683}{1179648}x^9 + \frac{11768319087087113}{1981808640}x^{10} \right], \quad (5)$$

with $x = \frac{J}{k_B T}$. Figure 3 depicts the fitting of $\chi(T)$ data in the validity $T$-range of Eq. (4), $k_B T > 8J$, corresponding to $T > 195$ K. Fixing $g = 2$ from the ESR data of Ref. [22], we obtain $J/k_B = (24 \pm 0.2)$ K and $\chi_0 = -(5.35 \pm 0.45) \times 10^{-5}$ cm$^3$/mol. An extension of the validity of the fit down to $T \sim 3.5J$ can be obtained using Padé approximants which are now available. The [6,5] Padé extension of our fit is shown as a dashed blue line in Fig. 3 and perfectly matches with our data in its validity domain, $T \gtrsim 85$ K, with $J/k_B = 24$ K and $\chi_0 = -5.35 \times 10^{-5}$ cm$^3$/mol.

## C. Heat Capacity

The heat capacity ($C_p$) data are shown in Fig. 4 (upper panel) as a function of temperature measured in zero magnetic field. At high temperatures, $C_p(T)$ is entirely dominated by the contribution of phonon excitations ($C_{ph}$) and the value of $C_p$ at 300 K is about $\sim 62$ J/mol K. This value is close to the expected Dulong-Petit lattice heat capacity of $C_v = 3nR \simeq 74.8$ J/mol K, where $n$ is the number of atoms per formula unit [45]. In $\alpha$-HCrO$_2$, H is the lightest element expected to have a very high Debye frequency compared to other elements, and therefore we chose $n = 3$ for the calculation. At around 24 K, the heat capacity shows a clear and very broad anomaly that confirms the magnetic transition. With further decrease in temperature, $C_p(T)$ decreases gradually towards zero. At low temperatures, $C_p(T)$ is dominated by the magnetic contribution $C_{mag}$.

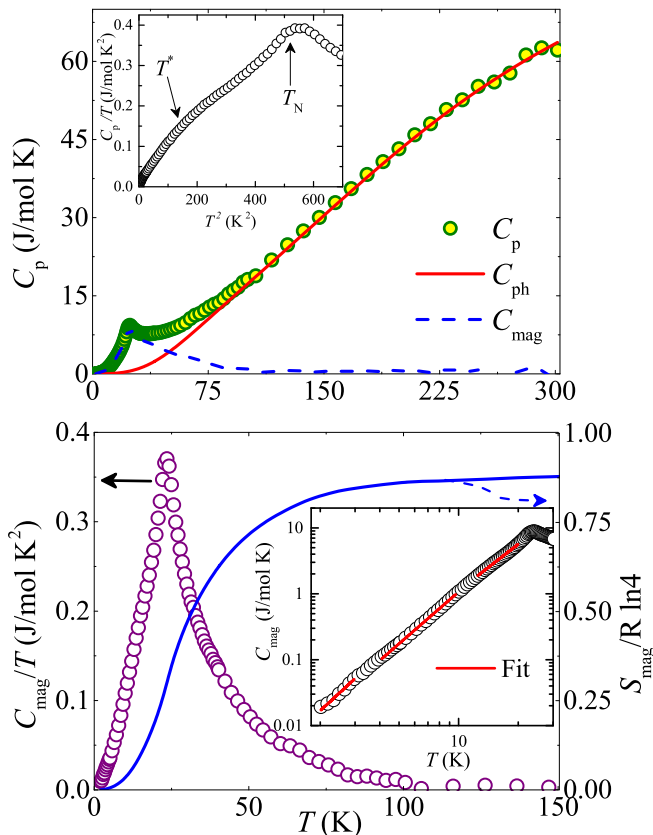In order to estimate the phonon part of the heat capacity, the $C_p(T)$ data were fitted above 100 K by a sum

FIG. 4. Upper panel: Temperature-dependent heat capacity $C_p(T)$ of $\alpha$-HCrO$_2$ measured in zero applied magnetic field. The solid line represents the simulated phonon contribution $C_{ph}(T)$ and the dashed line represents the magnetic contribution $C_{mag}(T)$. Inset: Plot of $C_p(T)/T$ vs $T^2$ below $T_N$, highlighting the shoulder at $T^* \simeq 12$ K. Lower panel: $C_{mag}/T$ and $S_{mag}/R\ln 4$ in the left and right $y$-axes, respectively, are plotted as a function of temperature. Inset: Logarithmic plot of $C_{mag}$ vs $T$, with solid lines showing the fits with a power-law, $C_{mag} = aT^\alpha$, in different temperature regimes.

of Debye contributions

$$C_p(T) = 9R \sum_{n=1}^{3} c_n \left(\frac{T}{\theta_{Dn}}\right)^3 \int_0^{\frac{\theta_{Dn}}{T}} \frac{x^4 e^x}{(e^x - 1)^2} dx. \quad (6)$$

Here, $R$ is the molar gas constant, $\theta_{Dn}$ are the characteristic Debye temperatures, and $c_n$ are the integer coefficients indicating the contributions of different atoms to $C_p(T)$. A similar approach has been chosen previously to estimate the phonon contribution in different types of frustrated magnets [46]. Figure. 4 (upper panel) presents the fit of $C_p(T)$ by Eq. (6) with $c_1 = 1$, $c_2 = 1$, and $c_3 = 2$. Here, $c_1$, $c_2$, and $c_3$ represent the number of H, Cr, and O atoms, respectively. The sum of $c_n$ is thus equal to 4, the number of atoms per formula unit. We have used three different Debye temperatures: $\theta_{D1}$ for H$^{1+}$, $\theta_{D2}$ for Cr$^{3+}$, and $\theta_{D3}$ for O$^{2-}$. Finally, the high-$T$ fit was extrapolated down to 2 K and $C_{mag}(T)$ was estimated by subtracting $C_{ph}(T)$ from $C_p(T)$ [see Fig. 4

(upper panel)].

$C_{mag}(T)/T$ is plotted as a function of temperature in the lower panel of Fig. 4. It extends up to 100 K, even though the leading exchange coupling $J$ is about 24 K only. For the validation of the fitting procedure, we calculated the total magnetic entropy ($S_{mag}$) by integrating $C_{mag}(T)/T$ between 2 K and high-temperatures as $S_{mag}(T) = \int_{2\,K}^{T} \frac{C_{mag}(T')}{T'} dT'$. The obtained magnetic entropy at 150 K is $S_{mag} \simeq 10.4$ J/mol K. This value of $S_{mag}$ corresponds to $\sim 90\%$ (see the lower panel of Fig. 4) of the expected theoretical value $S_{mag} = R\ln(2S+1) = 11.5$ J/mol K for a $S = 3/2$ system. Moreover, the entropy at $T_N$ is found to be only one-third of the total entropy and the remaining entropy is distributed above $T_N$ due to short-range (in-plane) spin correlations. This is in contrast with the conventional LRO where the entropy is recovered completely just above $T_N$, and confirms the strongly frustrated nature of $\alpha$-HCrO$_2$ [18, 47].

The broad maximum in $C_{mag}$ around 24 K confirms the magnetic transition, whereas a broad shoulder in $C_p/T$ vs $T^2$ (inset of the upper panel of Fig. 4) suggests another magnetic instability at $T^* \simeq 12$ K that coincides with the temperature at which the ZFC and FC susceptibilities bifurcate. This feature is quite similar to that reported for CuCrO$_2$ and $\alpha$-KCrO$_2$ previously [24, 48].

The logarithmic plot of $C_{mag}$ vs $T$ below $T_N$ (see, lower inset of Fig. 4) reveals a nearly linear behavior, although a closer inspection of the data suggests that different power-law exponents are obtained in different temperature intervals. Using $C_{mag} = aT^\alpha$, we find $a \simeq 0.0052$ J-mol$^{-1}$-K$^{-4}$ and $\alpha \simeq 2.2$ for 12.5 K$\leq T \leq 20$ K, $a \simeq 0.0026$ J-mol$^{-1}$-K$^{-4}$ and $\alpha \simeq 2.6$ for 4 K$\leq T \leq 10$ K, and $a \simeq 0.0025$ J-mol$^{-1}$-K$^{-4}$ and $\alpha \simeq 2.8$ for 2 K$\leq T \leq 3$ K. Considering $\alpha = 2$ and $\alpha = 3$ expected for antiferromagnets in 2D and 3D, respectively, we conclude that spin correlations gradually evolve from a 2D behavior immediately below $T_N$ toward a 3D behavior well below $T^*$.

### D. $^1$H NMR

The crystal structure of $\alpha$-HCrO$_2$ [Fig. 1(c)] features a single crystallographic H site located in between two Cr-triangles. The $^1$H nucleus is then coupled to three Cr$^{3+}$ ions from each of the two adjacent layers. Thus, one can probe static and dynamic properties of the Cr$^{3+}$ spins by performing $^1$H NMR. We have measured $^1$H NMR spectra by doing a Fourier Transform of the echo signal at different temperatures, keeping the field persistent. Figure 5 (upper panel) presents the FT $^1$H NMR spectra at different temperatures. We indeed observed a single spectral line, as expected for a $I = 1/2$ nucleus. The line position was found to increase weakly with decreasing temperature. The lower panel of Fig. 5 presents the temperature variation of the NMR shift ($K$) for $T > 30$ K. The slope of the linear fit using $K(T) = K_0 + \frac{A_{hf}}{N_A}\chi_{spin}(T)$ (where $K_0$ is the temperature-independent chemical shift) of the $K$ vs $\chi$ plot yields the
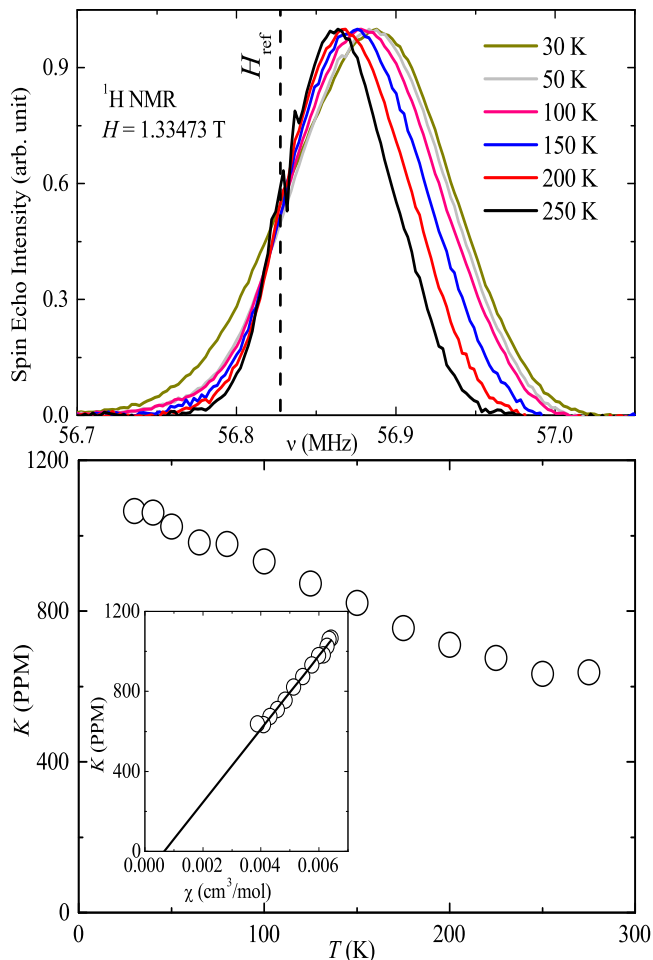
FIG. 5. Upper panel: FT $^1$H NMR spectra at different temperatures for the polycrystalline $\alpha$-HCrO$_2$ sample measured at $H = 1.33473$ T. The vertical dashed line corresponds to the $^1$H resonance frequency of the non-magnetic reference sample. Lower panel: $^1$H NMR shift $K$ as a function of $T$. Inset: $^1$H NMR shift vs $\chi$ with temperature as an implicit parameter. The solid line represents the linear fit.

hyperfine coupling constant $A_{hf} \simeq 1024$ Oe/$\mu_B$ between the $^1$H nucleus and the Cr$^{3+}$ electronic spins (see, inset of Fig. 5). This value of $A_{hf}$ is almost six times smaller than $^7$Li in LiCrO$_2$ [18, 21] but much larger than the expected dipolar coupling for $\alpha$-HCrO$_2$ [1]. The latter also indicates a substantial overlap of the hydrogen $1s$ orbital with the $3d$ orbitals of Cr$^{3+}$ ion via $2p$ orbitals of O. This further explains why the inter-layer exchange coupling through H is significant, as estimated in Sec. F.

Figure 6 shows the field-sweep NMR spectra around and below $T_N$. As the temperature approaches $T_N$ from above, the NMR signal intensity decreases. Below $T_N$, the signal is reduced drastically, whereas the line width does not show any significant increase. The loss of the NMR signal continues well below $T_N$ but never becomes complete, and below $\sim 10$ K the intensity quickly recovers. Below 10 K, the NMR line broadens and develops a
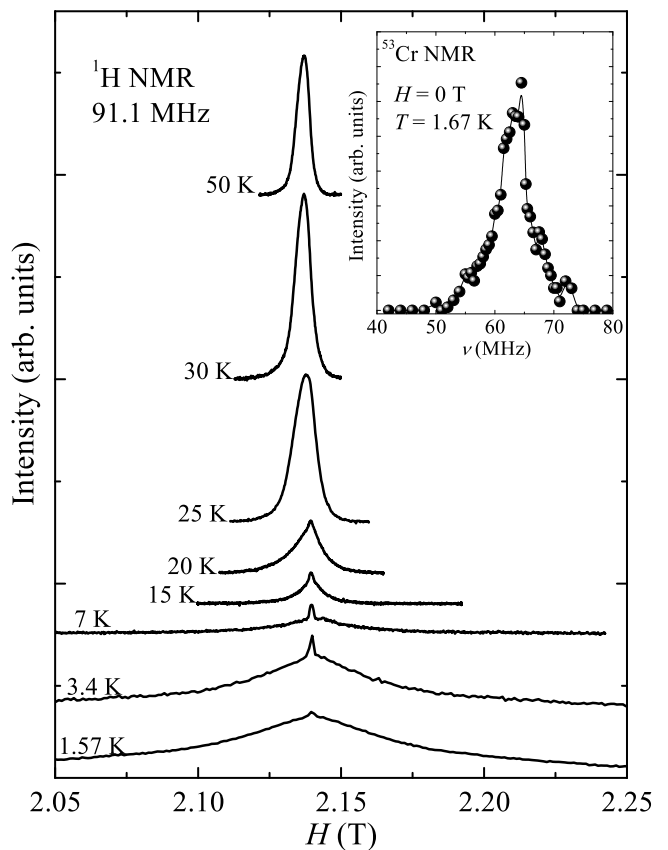


FIG. 6. Field-sweep $^1$H NMR spectra at different temperatures around $T_N$ measured on the polycrystalline $\alpha$-HCrO$_2$ sample at 91.1 MHz. Inset: $^{31}$Cr NMR spectrum at $T = 1.67$ K measured in zero field.

triangular shape which is independent of the applied field. This broadening is indicative of local magnetic fields appearing at the $^1$H site, but it is remarkable that such a broadening appears only below 10 K and not immediately below $T_N$, as in conventional 3D antiferromagnets. This is a clear indication that the NMR signal is wiped out over a broad temperature window, below $T_N$ and a pure static state appears only below 10 K. The wipe out effect is very well evident in the temperature dependent integrated NMR intensity plot in Fig. 7. A rectangular line shape on the polycrystalline sample is expected in an ordered collinear antiferromagnet [50, 51]. The triangular line shape observed at low temperatures in $\alpha$-HCrO$_2$ is reminiscent of an incommensurate magnetic order [52, 53] that may appear in triangular antiferromagnets upon a distortion of the commensurate 120° state. Further, as the intrinsic signal is lost below $T_N$ a very narrow central line becomes prominent at the zero shift position, on top of the broad spectrum. This narrow line persists down to the lowest measured temperature and can be attributed to the effect of defects and/or a small amount of non-magnetic impurities.

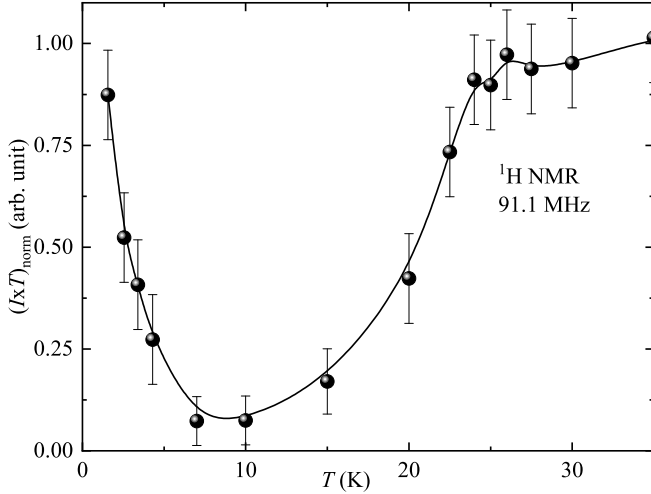We have also measured the $^{53}$Cr NMR ($I = 3/2$ and $\gamma_N/2\pi = 2.40094$ MHz/T) spectrum by sweeping the fre-

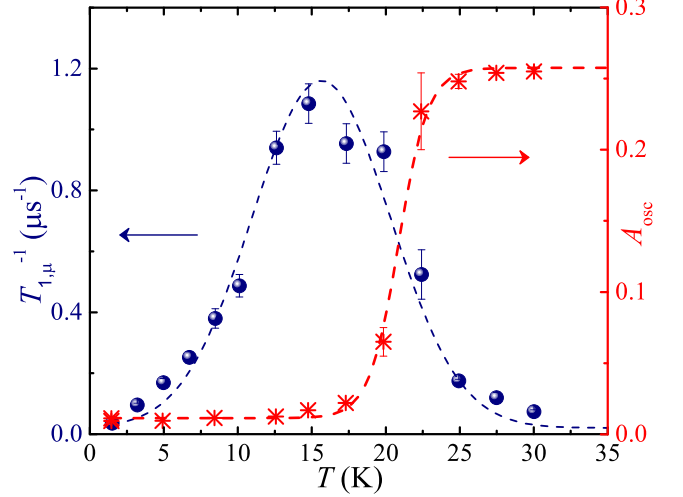FIG. 7. Integrated NMR intensity as a function of temperature.



FIG. 8. Left: $T$-variation of the muon relaxation rate; the dashed line is a guide to the eyes. Right: weak transverse field $\mu$SR asymmetry (see text). The dashed line is a fit to a phenomenological broadened "step" function $(A_{\text{tot}} - A_{\text{b}})/[1 + e^{((T_{\text{N}} - T)/\Delta T_{\text{N}})}] + A_{\text{b}}$.

quency in zero field at $T = 1.67$ K (see, inset of Fig. 6). The observation of $^{53}$Cr zero field NMR signal is a direct evidence of a static magnetic ordering of $Cr^{3+}$ moments in $\alpha$-HCrO$_2$ well below $T^*$. From the peak position, the internal field at the Cr site is estimated to be $|H_{\text{int}}| \sim 26.4$ T. Such a large value of $H_{\text{int}}$ is comparable to the reported value $\sim 28.64$ T for YCrO$_3$ and $\sim 27.0$ T for CuCrO$_2$ [54].

where $A_{\text{osc}}$ is the wTF oscillating asymmetry and $A_{\text{tail}}$ is introduced to account for the non-oscillating long-time relaxing frozen part ($1/3^{\text{rd}}$ tail). The fitted values for $A_{\text{osc}}$ are shown in Fig. 8 (right). An abrupt loss of asym-

### E.  $\mu$SR

In order to probe the dynamics in the fluctuating regime in more detail, we performed complementary $\mu$SR experiments. Owing to its much shorter time window (10 ns - 15 $\mu$s), $\mu$SR is better suited than NMR in tracking the persisting dynamics in slowly fluctuating magnets. In addition, $\mu$SR allows us to probe *all* sites, whereas only a weak fraction of the sites were detected in NMR between 20 and 3 K due to the wipeout effect.

$\mu$SR experiments under a weak applied field perpendicular to the initial muon spin polarization (wTF), were performed in order to track the spin freezing and the static magnetic volume fraction versus temperature. Indeed, only muons stopping close to paramagnetic (unfrozen) sites precess around the applied field direction and produce long-lived oscillations of the polarization reflected in the measured asymmetry. On the contrary, muons close to magnetically frozen parts experience much larger fields with a large distribution and yield a strongly damped contribution in the 0.1 $\mu$s range to the polarization as is evident in zero-field experiments presented next.

The wTF asymmetry was fitted using a standard function for $t > 0.5$ $\mu$s

$$A_{\text{wTF}}(t) = A_{\text{osc}} \cos(\gamma_\mu B_{\text{ext}} t + \phi)e^{-(\sigma^2 t^2/2)} + A_{\text{tail}}e^{-\lambda t}, \tag{7}$$
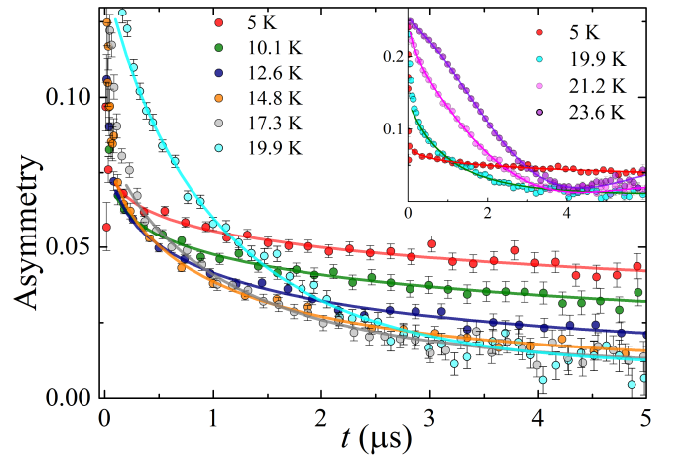


FIG. 9. $\mu$SR asymmetry in zero external field at various temperatures. The solid lines are fits described in the text.
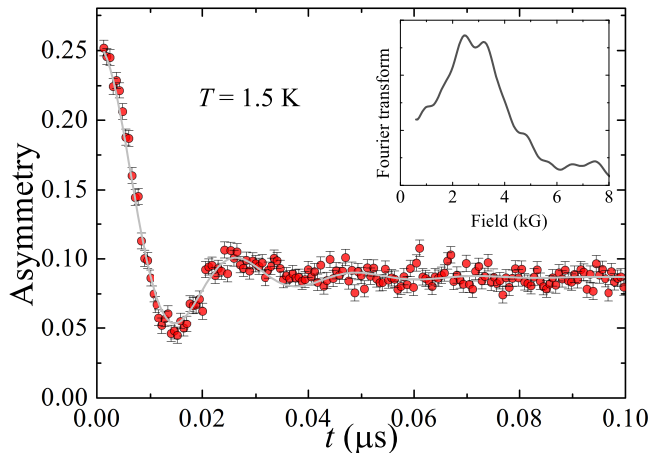
FIG. 10. Early-time $\mu$SR asymmetry in zero external field at 1.5 K and fit with a zero-order Bessel function $A[\frac{2}{3}J_0(t)e^{-\lambda t} + 1/3]$. Inset: Corresponding Fourier transform after subtraction of the $1/3^{\text{rd}}$ tail.

Fig. 9. Above $T_{\text{N}}$, in the fast fluctuation regime, muons mainly sense a weak $\sim 4.6$ G static nuclear magnetic field mainly originating from H nuclei. The decrease of the $\mu^+$ polarization has the expected Kubo-Toyabe shape, Gaussian at early times and modulated by a slowly exponential relaxing envelope associated with electronic spin fluctuations. When decreasing the temperature below $T_{\text{N}}$, similar to the NaCrO$_2$ case [21], the freezing of the electronic moments induces a very fast decrease of the asymmetry on a $0.1\mu$s range while the long-time $1/3^{\text{rd}}$ tail monitors the relaxation induced by the spin dynamics.

We first focus on the data obtained deep in the frozen regime. Figure 10 shows the very early time behavior of the asymmetry at 1.5 K. The oscillating behavior is made clear by the two visible wiggles and rules out a spinglass-like random freezing. The damping is very large, associated with a large distribution of the field at the muon site as depicted by the Fourier transform presented in the inset. Finally, one also observes the beginning of the $1/3^{\text{rd}}$ tail ($t > 0.06$ $\mu$s).

The $T = 1.5$ K asymmetry evolution with time was fitted according to the model:

$$A(t) = A_0 \left[ \frac{2}{3} P_{\text{osc}}(t) e^{-(\sigma'^2 t^2/2)} + \frac{1}{3} \right] e^{-(t/T_1)^\alpha} + A_b, \quad (8)$$

where $P_{\text{osc}}(t)$ is an oscillating function corresponding to the $\mu^+$ precession around the internal magnetic field ($B_\mu$) direction at the average frequency $\nu = (\gamma_\mu/2\pi)B_\mu$, while the damping of the oscillation is due to the width of the internal field distribution $\sigma'/\gamma_\mu$. The constant background, $A_b = 0.01$, was fixed from the remaining wTF asymmetry at $T \ll T_{\text{N}}$ and $A_0$ was set to $A_0 = A_{\text{tot}} - A_b$, with $A_{\text{tot}} = 0.255$, as determined from the total asymmetry fitted above $T_{\text{N}}$. We found a slightly better $\chi^2$ when fitting the oscillations with a Bessel function rather than a simple cosine. A $B_\mu \sim 2.75$ kG internal field is estimated from the frequency of the oscillations. The fast

early time damping reveals a large 1.4 kG HWHM distribution of $B_\mu$, either associated with an incommensurate order (Bessel fit) or a sizeable disorder (cosine fit). The flatness of the $1/3^{\text{rd}}$ tail on the timescale of Fig. 10, hence the weakness of the relaxation rate $1/T_1$, indicates a purely static magnetic frozen phase in the low-$T$ limit.

We now focus on the relaxation effects evidenced on the $1/3^{\text{rd}}$ tail at $t > 0.1 - 0.2$ $\mu$s as displayed in the main panel of Fig. 9. This was the central focus of our $\mu$SR study, given the wipe-out observed in NMR. For each temperature below 19.9 K, we could estimate the "unfrozen" contribution so that the asymmetry of the corresponding $1/3^{\text{rd}}$ tail was fixed from the wTF data. The asymmetry evolution with time was fitted using the following functions for $t > t_{1/3^{\text{rd}}}$ taken such that $A(t) \leq A_{\text{tail}}$ :

$$A(t) = A_{\text{tail}} \ e^{-t/T_1{}^\alpha} + A_b \quad (T < T_N) \qquad (9)$$

and

$$A(t) = A_0 \ \text{KT}(t) \ e^{-t/T_1{}^\alpha} + A_b \quad (T \gtrsim T_N), \qquad (10)$$

where KT$(t)$ is the Kubo-Toyabe function, Gausian like in the $t \to 0$ limit and $t_{1/3rd}$ is the time where the asymmetry falls to the value expected for the $1/3$rd tail, determined as $A_{\text{tail}} + A_b$, see above. The stretched exponent $\alpha$ was found to vary smoothly between 12 K and up to the transition from its low-$T$ value $\sim 0.3$ to 1. This indicates a broad distribution of relaxation times, in line with the distribution of internal fields reported in Fig. 10. The error bars mainly come from the estimate of $t > t_{1/3^{\text{rd}}}$, the error bars on the background and on the total asymmetry which slightly impact the relaxation rate. The fits were straightforward between 1.5 and 17.3 K where the "unfrozen fraction" is zero or marginal. For $T = 19.9$ K, the unfrozen part has a contribution to the relaxation which cannot be disentangled from the $1/3$rd tail. $A_{\text{tail}}$ was therefore replaced by $A_{\text{tail}} + A_{\text{osc}}$ in Eq. (9), leading to an average value of the relaxation rate. The increase of the relaxation rate is clearly visible, up to $T_1^{-1}(15$ K$) \sim 1$ $\mu$s$^{-1}$, followed by a decrease at $T = 17$ K (Fig. 8, left). The large $T$-range below $T_{\text{N}}$ where slow fluctuations occur, clearly signals an unconventional dynamical regime peaked around 0.7 $T_{\text{N}}$, at variance with the common phase transitions where the relaxation is peaked at $T_{\text{N}}$ [2].

### F. Microscopic Analysis

DFT calculations are used to identify the trends in the microscopic magnetic parameters across the $A$CrO$_2$ series. Exchange couplings and single-ion anisotropies computed for LiCrO$_2$, NaCrO$_2$, $\alpha$-KCrO$_2$, and for the two structural models of HCrO$_2$ are summarized in Table I. All compounds are dominated by the nearest-neighbor in-plane coupling $J_1$. This coupling is highly sensitive to the Cr–Cr distance $d$ and decreases from LiCrO$_2$

TABLE I. Exchange couplings $J_i$ (in K) and single-ion anisotropy $D$ (in K) obtained from DFT+$U$ calculations for the spin Hamiltonian, Eq. (1). $J_1$, $J_2$, and $J_3$ are in-plane couplings between first, second, and third neighbors, respectively. $J_\perp$ is the frustrated interplane coupling.

|  | $J_1$ | $J_2$ | $J_3$ | $J_\perp$ | $D$ |
|---|---|---|---|---|---|
| LiCrO$_2$ | 84 | −0.3 | 3.6 | 0.4 | 0.4 |
| NaCrO$_2$ | 48 | −0.5 | 2.7 | 0.1 | 0.6 |
| $\alpha$-KCrO$_2$ | 15 | 0.6 | 4.1 | 0.2 | 0.9 |
| $\alpha$-HCrO$_2$, $R\bar{3}m$ | 33 | −0.2 | 4.3 | 2.8 | 0.5 |
| $\alpha$-HCrO$_2$, $R3m$ | 28 | 1.0 | 4.3 | 2.0 | 0.5 |

TABLE II. Comparison of different structural and magnetic parameters of $ACrO_2$ ($A$ = H, Li, Na, and K) [58]. The exchange coupling $J$ (= $J_1$) for Li, Na, and K compounds is deduced using the HTSE given by Delmas et al [59] whereas for $\alpha$-HCrO$_2$, we have used $11^{th}$ order HTSE [Eq. (5)] suggested by Schmidt et al [43].

| Compounds | Interplanar spacing (Å) | $J$ (K) | $T_N$ (K) | Refs. |
|---|---|---|---|---|
| $\alpha$-HCrO$_2$ | 4.774 | 24 | 22.5 | this work |
| LiCrO$_2$ | 4.807 | 78 | 62 | [22, 24] |
| NaCrO$_2$ | 5.323 | 40 | 41 | [21, 22] |
| $\alpha$-KCrO$_2$ | 5.963 | 24 | 23 | [24, 60] |

($d$ = 2.901 Å) to NaCrO$_2$ ($d$ = 2.975 Å) and eventually $\alpha$-KCrO$_2$ ($d$ = 3.044 Å). The $J_1$ value in $\alpha$-HCrO$_2$ lies in between those of the Na and K compounds, despite its Cr–Cr distance of 2.968 Å, which is slightly shorter than in the Na case. This additional reduction in the $J_1$ value may be caused by the hydrogen atoms that are placed next to oxygen and change its polarization [56]. The exact position of hydrogen along the O–H–O contact ($R\bar{3}m$ vs $R3m$ models) plays only a minor role, as evident from Table I.

The computed values of $J_1$ are generally in good agreement with the experimental estimates based on the magnetic susceptibility data (Table II). The coupling in LiCrO$_2$ is also in accord with the spectroscopic measurements of magnetic excitations [57] that suggested $J_1 \simeq 70$ K (6.0 meV).

A weak easy-axis single-ion anisotropy ($D$) is present in all compounds and does not change significantly across the series. Indeed, the calculated value of $D$ for $\alpha$-KCrO$_2$ matches well with the value estimated from the ESR experiments (see, Supplementary Materials [41]). On the other hand, the interlayer coupling $J_\perp$ notably increases in $\alpha$-HCrO$_2$, owing to the reduced interlayer spacing (Table II) and the covalent nature of the O–H bonds as opposed to the purely ionic bonding between alkali metals (Li, Na, K) and oxygen.
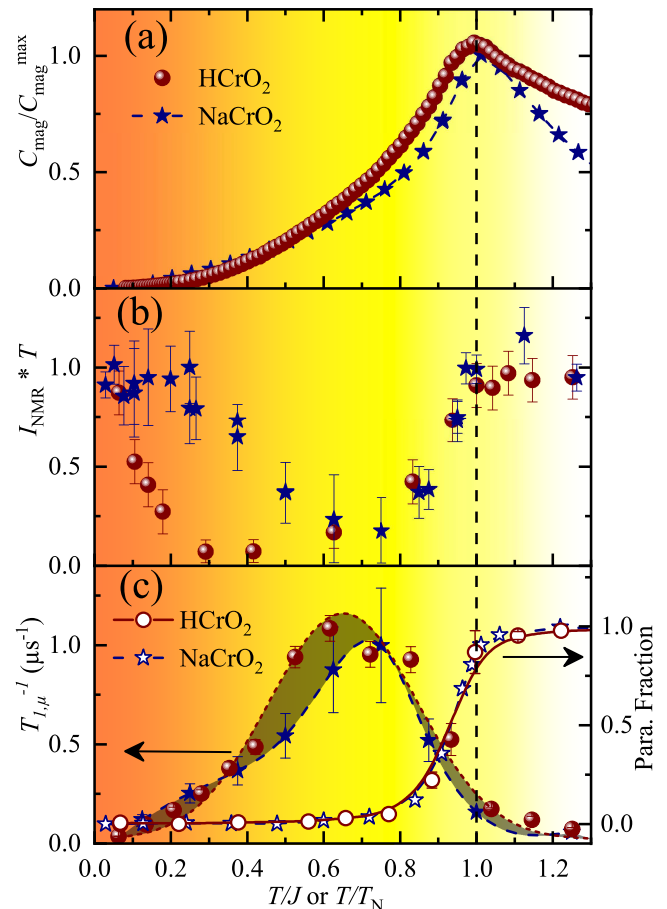


FIG. 11. Comparison of low temperature data of $\alpha$-HCrO$_2$ with NaCrO$_2$; (a) magnetic heat capacity normalized to its maximum value vs $T/J$ (b) evaluation of integrated NMR intensity with $T/J$, and (c) $\mu$SR relaxation rate $1/T_{1,\mu}$ vs $T/J$ and the paramagnetic fraction vs $T/T_N$ in the left and right $y$-axes, respectively. Here the transition temperature is taken to be $T_N \simeq 22.5$ K and 41 K for $\alpha$-HCrO$_2$ and NaCrO$_2$, respectively.

## IV. DISCUSSION

This discussion section is divided into two parts: the first part is devoted to a discussion on the transition temperature with respect to frustration. The second part is devoted to the extended dynamical regime below the transition which is found to have a universal character among the $ACrO_2$ ($A$=H, Na, and K) series of chromates.

For a purely 2D triangular Heisenberg antiferromagnet, one would expect a transition only at $T = 0$ into a three-sublattice structure with spins at 120°. In the presence of a weak interlayer exchange coupling, the transition is still mainly driven by the growth of the 2D correlation length $\xi(T)$ when cooling down: it diverges at $T = 0$. Indeed, in a mean-field approach, the transition is obtained by equating the thermal energy to the interaction of 2D correlated patches through a small interlayer exchange coupling. This can be approached by

the following mean-field equation that leads to a finite transition temperature,

$$k_B T_N \sim J_\perp S^2 [\xi(T_N)/a]^2. \quad (11)$$

From Refs. [61, 62] we get

$$\xi(T) \sim (T/J)^{-0.5} \exp(\alpha J/T). \quad (12)$$

One can then expect a transition temperature modestly increasing with $J_\perp$. From Tables I and II, one can notice that $J_\perp$ decreases when the inter-layer distance increases from $\alpha$-HCrO$_2$ to $\alpha$-KCrO$_2$, as expected, and $J_\perp$ is more than a factor 15-30 larger for $\alpha$-HCrO$_2$ as compared to NaCrO$_2$ and $\alpha$-KCrO$_2$. While the $J/T_N$ ratio is similar or even slightly larger for $\alpha$-HCrO$_2$, the transition temperature surprisingly does not scale at all with $J_\perp$. We suggest that this failure of the mean field, well-established, approach for low-dimensional systems can be assigned to a peculiar degree of interlayer frustration in $\alpha$-HCrO$_2$. Indeed, we first note that the geometry of the inter-layer coupling [see Fig. 1(b)] leads to some frustration through the *tetrahedral* units resulting from the *ABC* type of stacking, common to all the chromates mentioned above: one Cr$^{3+}$ is coupled to six Cr$^{3+}$ from the two adjacent layers. Second, a higher degree of frustration induced by the interlayer coupling, as found for $\alpha$-HCrO$_2$, certainly prevents the correlation length to grow according to Eq. (12) which leads to the apparent paradox of "a larger $J_\perp$ yields to a lower $T_N$". We note that this frustration scenario is in line with the incommensurate structure observed at 1.57 K through the NMR lineshape and also consistent with the $\mu$SR time-evolution of the asymmetry at 1.5 K.

Now, coming to the intermediate $T$-range below $T_N$, several of the $A$CrO$_2$ compounds show a very similar phenomenology. In Fig. 11, we compare our results to those obtained in NaCrO$_2$ [21], using $J$ as a scaling parameter.
(*i*) Both $\alpha$-HCrO$_2$ and NaCrO$_2$ undergo a magnetic transition that manifests itself in the heat capacity and $\mu$SR, but does not lead to the formation of a conventional 3D transition with a narrow critical regime centered in the vicinity of $T_N$. On the contrary, here the transition at $T_N$ is followed by a broad regime with slow fluctuations peaked around 0.6-0.7 $T_N$ [Fig. 11(c)]. Strikingly, this maximum largely coincides with the bifurcation point of the FC/ZFC susceptibility reported at 12-15 K in Fig. 3 for $\alpha$-HCrO$_2$. The extension of this regime can be tracked through the $\mu$SR relaxation rate, which shows a striking similarity in both compounds once the temperatures are normalized by $J$.
(*ii*) The heat capacity also displays a very broad maximum around $T_N$ and a similar behavior below $T_N$ for both compounds when the temperature axis is scaled by their respective $J$.
(*iii*) For both compounds, the intensity of the NMR line progressively decreases, goes through a minimum, and recovers below a temperature $T^*$ where slow fluctuations detected through $\mu$SR freeze out [3].

Similar plots including the data taken on $\alpha$-KCrO$_2$ can be found in the supplementary materials [41], they clearly demonstrate the universal character of this scaling in $T/J$ for that series of chromates.

We are therefore led to the conclusion that a broad universal dynamical regime emerges on a $T/J$ scale, typical of *ABC*-stacked triangular Heisenberg antiferromagnets and characterized by a very progressive slowing down of spin fluctuations.

Neutron scattering studies offered a possible explanation for this unusual behavior as reported earlier for NaCrO$_2$ [64–66]. Between 1.3 and 0.7 $T_N$, the in-plane correlation length grows rapidly with a $\vec{q}$ vector typical of the 120° pattern. On the contrary, the inter-layer correlation length increases very progressively from 1 inter-layer spacing at $T_N$ to only 4 inter-layer spacings at 0.7 $T_N$ where it levels off. This $T$-range closely below $T_N$ is dominated by 2D correlations.

The increase in $1/T_{1,\mu}$ up to its maximum could be such a hallmark of the 2D regime, in fair agreement with the $T^2$ behavior of the specific heat that we clearly observe in $\alpha$-HCrO$_2$. At lower temperatures, a release of the inter-layer frustration through a small incommensuration may strengthen the 3D coupling. The consequence is a progressive slowing down of the fluctuations as observed in $\mu$SR. This regime is typical of a 2D-3D crossover. What remains unclear is certainly the universality observed in the maximum of $1/T_{1,\mu}$. It might be a coincidental result of two counteracting mechanisms driven by $J_\perp$, namely, an increase of both the coupling and the frustration between the layers.

Alternative scenarios, namely, the Berezinskii-Kosterlitz-Thouless (BKT) scenario of vortex-antivortex binding or that of $Z_2$ vortex excitations, have been proposed for NaCrO$_2$ [21, 22]. Indeed the maximum in the $\mu$SR relaxation rate at $T_m \simeq 0.7 T_N$ was found to coincide with the divergence of the correlation length inferred from the broadening of the ESR line according to the BKT model, $\xi(T) \sim \exp \frac{b}{T-T_m}$. The data now available on $\alpha$-HCrO$_2$ and $\alpha$-KCrO$_2$ prove the failure of this scaling in $T/T_m$ (see, Supplementary Materials [41] for the tentative scaling) and rules out such an interpretation. In addition, we note that a BKT scenario requires a substantial XY anisotropy, which has never been observed experimentally. This, therefore, calls for a different interpretation of the ESR line broadening in terms of a growth of the correlation length when entering the 3D regime.

A more general lesson from the $A$CrO$_2$ chromates is that the fluctuating 2D regime clearly sets in below $T_N$, likely from the interlayer frustration. This offers a new perspective on the persistent spin dynamics and other spin-liquid phenomenology such as observed in the $A$Yb$X_2$ compounds [15, 16] where exchange anisotropy also certainly plays a role. It also calls for the improved theoretical understanding of how deep the frustration of weak interlayer couplings may affect the ground state of a quasi-2D antiferromagnet. Our experimental data for

the pure Heisenberg triangular chromates set an important benchmark for such studies.

In conclusion, besides the observation of a Néel transition, features reminiscent of the pure 2D Heisenberg triangular lattice are manifested through the dynamics as revealed here experimentally, between $T_N$ and 0.7 $T_N$. The study of the $ACrO_2$ chromates ($A$ = H, Na, and K) points to an original and universal character of excitations. With their half filled $t_{2g}$ orbitals, chromates are certainly the best representative of a semi-classical $S = 3/2$ Heisenberg model. The perfection of the equilateral triangular lattice with nearly no disorder is a strong asset to provide a solid playground for the physics of frustration at play on the triangular lattice in a context where more disordered compounds such as $YbMgGaO_4$ or $AYbX_2$ QSL candidates are in the spotlight. Certainly, the interpretation of the 2D-3D crossover resides in the details of each of these compounds although the universal plot in $T/J$ might suggest that it is still governed by the dynamics specific to the 2D frustrated character of the triangular lattice.

## V. SUMMARY

The static and dynamic properties of spin-3/2 TLHAF $\alpha$-HCrO$_2$ are studied in detail and compared with the iso-structural compounds (Na,K)CrO$_2$. $\chi(T)$ could be modeled using HTSE for spin-3/2 TLHAF which yields an intra-layer coupling $J/k_B \simeq 24$ K. The complementary band structure calculations result in a similar value of $J$. They additionally provide a sizable inter-layer coupling $J_\perp/k_B \simeq 2.8$ K which appears specific to $\alpha$-HCrO$_2$. This brings in inter-layer frustration which shifts down the transition temperature as compared to other members of the chromates series. On the experimental side, a large hyperfine coupling $A_{hf} \simeq 1021$ Oe/$\mu_B$ between the $^1$H nuclei and the Cr$^{3+}$ spins corroborate the existence of such a sizable inter-layer coupling.

Although, $\chi(T)$, $C_p(T)$ and muon asymmetry measurements reveal the onset of a magnetic transition at $T_N$, which is also monitored through a magnetoelastic coupling, a wide fluctuating crossover regime marked by

a broad peak in the muon relaxation rate $1/T_{1,\mu}$ centered at $T \simeq 0.7$ $T_N$ and a minimum in the $^1$H NMR integrated intensity is singled out. Apparently, this slow dynamical regime turns out to be a universal character of the TLHAFs $ACrO_2$ ($A$ = Na, K, and H) when the specific heat, NMR intensity, $1/T_{1,\mu}$, and paramagnetic fraction are plotted against the scaled (with respect to $J$ or $T_N$) temperature. This supports a scenario where a crossover from 2D to 3D correlations sets in around 0.7 $T_N$ preceded by a typical 2D regime of the TLHAF.

## ACKNOWLEDGMENTS

[1] C. Broholm, R. J. Cava, S. A. Kivelson, D. G. Nocera, M. R. Norman, and T. Senthil, Quantum spin liquids, Science **367**, eaay0668 (2020).

[2] J. Knolle and R. Moessner, A field guide to spin liquids, Ann. Rev. Condens. Matter Phys. **10**, 451 (2019).

[3] X.-G. Wen, Choreographed entanglement dances: Topological states of quantum matter, Science **363**, eaal3099 (2019).

[4] J. R. Chamorro, T. M. McQueen, and T. T. Tran, Chemistry of quantum spin liquids, Chem. Rev. **121**, 2898 (2021).

[5] P. Mendels and F. Bert, Quantum kagome frustrated antiferromagnets: One route to quantum spin liquids, C. R. Phys. **17**, 455 (2016).

[6] Y. Li, P. Gegenwart, and A. A. Tsirlin, Spin liquids in geometrically perfect triangular antiferromagnets, J. Phys.: Condens. Matter **32**, 224004 (2020).

[7] S. M. Winter, A. A. Tsirlin, M. Daghofer, J. van den Brink, Y. Singh, P. Gegenwart, and R. Valentí, Models and materials for generalized Kitaev magnetism, J. Phys.: Condens. Matter **29**, 493002 (2017).

[8] W. W. Liu, Z. Zhang, J. T. Ji, Y. X. Liu, J. S. Li, X. Wang, H. Lei, G. Chen, and Q. M. Zhang, Rare-earth chalcogenides: A large family of triangular lattice spin liquid candidates, Chin. Phys. Lett. **35**, 117501 (2018).

[9] M. Baenitz, P. Schlender, J. Sichelschmidt, Y. A. Onykiienko, Z. Zangeneh, K. M. Ranjith, R. Sarkar, L. Hozoi, H. C. Walker, J.-C. Orain, H. Yasuoka, J. van den Brink, H. H. Klauss, D. S. Inosov, and T. Doert, $NaYbS_2$: A planar spin-$\frac{1}{2}$ triangular-lattice magnet and putative spin liquid, Phys. Rev. B **98**, 220409(R) (2018).

[10] K. M. Ranjith, D. Dmytriieva, S. Khim, J. Sichelschmidt, S. Luther, D. Ehlers, H. Yasuoka, J. Wosnitza, A. A. Tsirlin, H. Kühne, and M. Baenitz, Field-induced instability of the quantum spin liquid ground state in the $J_{\text{eff}} = \frac{1}{2}$ triangular-lattice compound $NaYbO_2$, Phys. Rev. B **99**, 180401(R) (2019).

[11] K. M. Ranjith, S. Luther, T. Reimann, B. Schmidt, P. Schlender, J. Sichelschmidt, H. Yasuoka, A. M. Strydom, Y. Skourski, J. Wosnitza, H. Kühne, T. Doert, and M. Baenitz, Anisotropic field-induced ordering in the triangular-lattice quantum spin liquid $NaYbSe_2$, Phys. Rev. B **100**, 224417 (2019).

[12] R. Sarkar, P. Schlender, V. Grinenko, E. Haeussler, P. J. Baker, T. Doert, and H.-H. Klauss, Quantum spin liquid ground state in the disorder free triangular lattice $NaYbS_2$, Phys. Rev. B **100**, 241116(R) (2019).

[13] M. M. Bordelon, C. Liu, L. Posthuma, P. M. Sarte, N. P. Butch, D. M. Pajerowski, A. Banerjee, L. Balents, and S. D. Wilson, Spin excitations in the frustrated triangular lattice antiferromagnet $NaYbO_2$, Phys. Rev. B **101**, 224427 (2020).

[14] P.-L. Dai, G. Zhang, Y. Xie, C. Duan, Y. Gao, Z. Zhu, E. Feng, Z. Tao, C.-L. Huang, H. Cao, A. Podlesnyak, G. E. Granroth, M. S. Everett, J. C. Neuefeind, D. Voneshen, S. Wang, G. Tan, E. Morosan, X. Wang, H.-Q. Lin, L. Shu, G. Chen, Y. Guo, X. Lu, and P. Dai, Spinon Fermi surface spin liquid in a triangular lattice antiferromagnet $NaYbSe_2$, Phys. Rev. X **11**, 021044 (2021).

[15] L. Ding, P. Manuel, S. Bachus, F. Grußler, P. Gegenwart, J. Singleton, R. D. Johnson, H. C. Walker, D. T. Adroja, A. D. Hillier, and A. A. Tsirlin, Gapless spin-liquid state in the structurally disorder-free triangular antiferromagnet $NaYbO_2$, Phys. Rev. B **100**, 144432 (2019).

[16] M. M. Bordelon, E. Kenney, C. Liu, T. Hogan, L. Posthuma, M. Kavand, Y. Lyu, M. Sherwin, N. P. Butch, C. Brown, M. J. Graf, L. Balents, and S. D. Wilson, Field-tunable quantum disordered ground state in the triangular-lattice antiferromagnet $NaYbO_2$, Nature Phys. **15**, 1058 (2019).

[17] H. Kadowaki, H. Takei, and K. Motoya, Double-Q $120°$ structure in the Heisenberg antiferromagnet on rhombohedrally stacked triangular lattice $LiCrO_2$, J. Phys. Condens. Matter **7**, 6869 (1995).

[18] L. K. Alexander, N. Büttgen, R. Nath, A. V. Mahajan, and A. Loidl, $^7Li$ NMR studies on the triangular lattice system $LiCrO_2$, Phys. Rev. B **76**, 064429 (2007).

[19] J. Sugiyama, M. Månsson, Y. Ikedo, T. Goko, K. Mukai, D. Andreica, A. Amato, K. Ariyoshi, and T. Ohzuku, $\mu^+SR$ investigation of local magnetic order in $LiCrO_2$, Phys. Rev. B **79**, 184411 (2009).

[20] A. Olariu, P. Mendels, F. Bert, L. K. Alexander, A. V. Mahajan, A. D. Hillier, and A. Amato, Spin dynamics in Heisenberg triangular antiferromagnets: A $\mu SR$ study of $LiCrO_2$, Phys. Rev. B. **79**, 224401 (2009).

[21] A. Olariu, P. Mendels, F. Bert, B. G. Ueland, P. Schiffer, R. F. Berger, and R. J. Cava, Unconventional Dynamics in Triangular Heisenberg Antiferromagnet $NaCrO_2$, Phys. Rev. Lett. **97**, 167203 (2006).

[22] M. Hemmida, H.-A. Krug von Nidda, N. Büttgen, A. Loidl, L. K. Alexander, R. Nath, A. V. Mahajan, R. F. Berger, R. J. Cava, Y. Singh, and D. C. Johnston, Vortex dynamics and frustration in two-dimensional triangular chromium lattices, Phys. Rev. B. **80**, 054406 (2009).

[23] J. Liu, B. Liu, L. Yuan, B. Li, L. Xie, X. Chen, H. Zhang, D. Xu, W. Tong, J. Wang, and Y. Li, Frustrated magnetism of the triangular-lattice antiferromagnets $\alpha$-CrOOH and $\alpha$-CrOOD, New J. Phys. **23**, 033040 (2021).

[24] F. Xiao, T. Lancaster, P. J. Baker, F. L. Pratt, S. J. Blundell, J. S. Möller, N. Z. Ali, and M. Jansen, Magnetic transition and spin dynamics in the triangular Heisenberg antiferromagnet $\alpha$-KCrO$_2$, Phys. Rev. B. **88**, 180401 (2013).

[25] Amato, A. and Luetkens, H. and Sedlak, K. and Stoykov, A. and Scheuermann, R. and Elender, M. and Raselli, A. and Graf, D., The new versatile general purpose surface-muon instrument (GPS) based on silicon photomultipliers for $\mu^+SR$ measurements on a continuous-wave beam, Rev. Sci. Instruments **88**, 093301 (2017).

[26] K. Koepernik and H. Eschrig, Full-potential nonorthogonal local-orbital minimum-basis band-structure scheme, Phys. Rev. B **59**, 1743 (1999).

[27] J. P. Perdew, K. Burke, and M. Ernzerhof, Generalized Gradient Approximation Made Simple, Phys. Rev. Lett. **77**, 3865 (1996).

[28] O. Janson, S. Chen, A. A. Tsirlin, S. Hoffmann, J. Sichelschmidt, Q. Huang, Z.-J. Zhang, M.-B. Tang, J.-T. Zhao, R. Kniep, and H. Rosner, Structure and magnetism of $Cr_2[BP_3O_{12}]$: Towards the quantum-classical crossover in a spin-3/2 alternating chain, Phys. Rev. B **87**, 064417 (2013).

[29] O. Janson, G. Nénert, M. Isobe, Y. Skourski, Y. Ueda, H. Rosner, and A. A. Tsirlin, Magnetic pyroxenes $LiCrGe_2O_6$ and $LiCrSi_2O_6$: Dimensionality crossover in a nonfrustrated $S = \frac{3}{2}$ Heisenberg model, Phys. Rev. B **90**, 214424 (2014).

[30] Z. Lu and J. R. Dahn, Structure and Electrochemistry of Layered $Li[Cr_xLi_{(1/3-x/3)}Mn_{(2/3-2x/3)}]O_2$, J. Electrochem. Soc. **149**, A1454 (2002).

[31] W. Scheld and R. Hoppe, Über den $\alpha$-NaFeO$_2$-Typ: Zur Kenntnis von $NaCrO_2$ und $KCrO_2$, Z. anorg. allg. Chem. **568**, 151 (1989).

[32] M. Ichikawa, T. Gustafsson, I. Olovsson, and T. Tsuchida, Powder neutron-diffraction profile analysis of zero-dimensional H-bonded crystal $HCrO_2$, J. Phys. Chem. Solids. **60**, 1875 (1999).

[33] H. J. Xiang, E. J. Kan, S.-H. Wei, M.-H. Whangbo, and X. G. Gong, Predicting the spin-lattice order of frustrated systems from first principles, Phys. Rev. B **84**, 224429 (2011).

[34] J. Rodríguez-Carvajal, Recent advances in magnetic structure determination by neutron powder diffraction, Physica B **192**, 55 (1993).

[35] T. Chatterji, B. Ouladdiaf, P. F. Henry, and D. Bhattacharya, Magnetoelastic effects in multiferroic $YMnO_3$, J. Phys.: Condens. Matter **24**, 336003 (2012).

[36] S. Reschke, A. A. Tsirlin, N. Khan, L. Prodan, V. Tsurkan, I. Kézsmárki, and J. Deisenhofer, Structure, phonons, and orbital degrees of freedom in $Fe_2Mo_3O_8$, Phys. Rev. B **102**, 094307 (2020).

[37] S. S. Islam, K. M. Ranjith, M. Baenitz, Y. Skourski, A. A. Tsirlin, and R. Nath, Frustration of square cupola in $Sr(TiO)Cu_4(PO_4)_4$, Phys. Rev. B. **97**, 174432 (2018).

[38] R. G. Meisenheimer and J. D. Swalen, Magnetic Properties of $HCrO_2$ and $DCrO_2$, Phys. Rev. **123**, 831 (1961).

[39] J. A. Ibers, C. H. Holm, and C. R. Adams, Proton Magnetic Resonance Study of Polycrystalline $HCrO_2$, Phys. Rev. **121**, 1620 (1961).

[40] T. Matsuo, T. Maekawa, A. Inaba, O. Yamamuro, M. Ohama, M. Ichikawa, and T. Tsuchida, Isotope-dependent crystalline phases at ambient temperature: Spectroscopic and calorimetric evidence for a deuteration-induced phase transition at 320 K in $\alpha$-$DCrO_2$, J. Mol. Struct. **790**, 129 (2006), horizons in Hydrogen Bond Research 2005.

[41] See Supplemental Material at http: LINK for additional information, which includes Refs. [22, 67–74].

[42] C. Domb and A. R. Miedema, *J. Low Temp. Phys.*, Vol. 4 (edited by C. J. Gorter, North Holland. Amsterdam, 1964).

[43] H.-J. Schmidt, A. Lohmann, and J. Richter, Eighth-order high-temperature expansion for general heisenberg hamiltonians, Phys. Rev. B **84**, 104443 (2011).

[44] A. Lohmann, H.-J. Schmidt, and J. Richter, Tenth-order high-temperature expansion for the susceptibility and the specific heat of spin-$s$ Heisenberg models with arbitrary exchange patterns: Application to pyrochlore and kagome magnets, Phys. Rev. B **89**, 014415 (2014).

[45] R. K. Fitzgerel and F. H. Verhoek, The law of Dulong and Petit, J. Chem. Educ **37**, 545 (1960).

[46] N. Ahmed, A. A. Tsirlin, and R. Nath, Multiple magnetic transitions in the spin-$\frac{1}{2}$ chain antiferromagnet $SrCuTe_2O_6$, Phys. Rev. B. **91**, 214413 (2015).

[47] H. Takatsu, H. Yoshizawa, S. Yonezawa, and Y. Maeno, Critical behavior of the metallic triangular-lattice Heisenberg antiferromagnet $PdCrO_2$, Phys. Rev. B **79**, 104424 (2009).

[48] T. Okuda, Y. Beppu, Y. Fujii, T. Onoe, N. Terada, and S. Miyasaka, Specific heat of delafossite oxide $CuCr_{1-x}Mg_xO_2$ $(0 \leq x \leq 0.03)$, Phys. Rev. B **77**, 134423 (2008).

[1] The dipolar coupling constant at the H site is calculated using lattice sum with an assumption of $1\mu_B$ magnetic moment on each $Cr^{3+}$ ion to be $\sim 0.150$ kOe/$\mu_B$ per $Cr^{3+}$ ion.

[50] J. Kikuchi, K. Ishiguchi, K. Motoya, M. Itoh, K. Inari, N. Eguchi, and J. Akimitsu, NMR and Neutron Scattering Studies of Quasi One-Dimensional Magnet $CuV_2O_6$, J. Phys. Soc. Jpn. **69**, 2660 (2000).

[51] R. Nath, K. M. Ranjith, B. Roy, D. C. Johnston, Y. Furukawa, and A. A. Tsirlin, Magnetic transitions in the spin-$\frac{5}{2}$ frustrated magnet $BiMn_2PO_6$ and strong lattice softening in $BiMn_2PO_6$ and $BiZn_2PO_6$ below 200 K, Phys. Rev. B. **90**, 024431 (2014).

[52] M. Kontani, T. Hioki, and Y. Masuda, Hyperfine fields in an incommensurate antiferromagnetic Cr-Mo alloy system, J. Phys. Soc. Jpn. **39**, 672 (1975).

[53] K. Ranjith, R. Nath, M. Majumder, D. Kasinathan, M. Skoulatos, L. Keller, Y. Skourski, M. Baenitz, and A. Tsirlin, Commensurate and incommensurate magnetic order in spin-1 chains stacked on the triangular lattice in $Li_2NiW_2O_8$, Phys. Rev. B. **94**, 014415 (2016).

[54] H. Takeda, Y. Shimizu, M. Itoh, M. Isobe, and Y. Ueda, Local electronic state in the high-valence hollandite-type chromium oxide $K_2Cr_8O_{16}$ investigated by $^{53}Cr$ NMR, Phys. Rev. B **88**, 165107 (2013); A. G. Smol'nikov, V. V. Ogloblichev, S. V. Verkhovskii, K. N. Mikhalev, A. Y. Yakubovskii, K. Kumagai, Y. Furukawa, A. F. Sadykov, Y. V. Piskunov, A. P. Gerashchenko, S. N. Barilo, and S. V. Shiryaev, $^{53}Cr$ NMR study of $CuCrO_2$ multiferroic, JETP Letters **102**, 674 (2015).

[2] Note that the ratio of the NMR and $\mu$ SR relaxation rates $(1/T_1)_{NMR}/(1/T_1)_{\mu SR}$ scales with the ratio of the coupling constants squared. An order of magnitude can be calculated from the ratio of $\mu$SR internal field found at 1.5 K and the product of the hyperfine constant by the $Cr^{3+}$ moment, assumed to be $3.87\mu_B$ or accordingly from the 5 kG HWHM of the NMR spectrum at 1.5 K. At 15 K, this yields a rough estimate of $(T_1)_{NMR}$, of the order of 9-25 $\mu$s, which explains well the wipe-out.

[56] S. Lebernegg, A. A. Tsirlin, O. Janson, and H. Rosner, Two energy scales of spin dimers in clinoclase $Cu_3(AsO_4)(OH)_3$, Phys. Rev. B **87**, 235117 (2013).

[57] S. Tóth, B. Wehinger, K. Rolfs, T. Birol, U. Stuhr, H. Takatsu, K. Kimura, T. Kimura, H. M. Rønnow, and C. Rüegg, Electromagnon dispersion probed by inelastic X-ray scattering in $LiCrO_2$, Nature Comm. **7**, 13547 (2016).

[58] S. Angelov and J. Doumerc, On the correlation between the structure and the exchange interactions in $ACrO_2$ chromites, Solid State Commun. **77**, 213 (1991).

[59] J.-P. Doumerc, A. Wichainchai, A. Ammar, M. Pouchard, and P. Hagenmuller, On magnetic properties of some oxides with delafossite-type structure, Mater. Res. Bull. **21**, 745 (1986).

[60] N. Zafar Ali, J. Nuss, and M. Jansen, A New Polymorph of Potassium Chromate(III), $\beta$-$KCrO_2$, and Reinvestigation of $\alpha$-$KCrO_2$, Z. Anorg. Allg. Chem **639**, 241 (2013).

[61] P. Azaria, B. Delamotte, and D. Mouhanna, Low-temperature properties of two-dimensional frustrated quantum antiferromagnets, Phys. Rev. Lett. **68**, 1762 (1992).

[62] N. Elstner, R. R. P. Singh, and A. P. Young, Finite temperature properties of the spin-1/2 Heisenberg antiferromagnet on the triangular lattice, Phys. Rev. Lett. **71**, 1629 (1993).

[3] Note that the difference in the extension of this regime can be due in the way extrapolations of transverse relaxation $T_2$ plots have been performed which is always fairly delicate when $T_2$ is short.

[64] D. Hsieh, D. Qian, R. F. Berger, R. J. Cava, J. W. Lynn, Q. Huang, and M. Z. Hasan, Magnetic excitations in triangular lattice $NaCrO_2$, J. Phys. Chem. Solids **69**, 3174 (2008).

[65] D. Hsieh, D. Qian, R. F. Berger, R. J. Cava, J. W. Lynn, Q. Huang, and M. Z. Hasan, Unconventional spin order in the triangular lattice system $NaCrO_2$: A neutron scattering study, Physica B **403**, 1341 (2008).

[66] D. Hsieh, D. Qian, R. F. Berger, C. Liu, B. Ueland, P. Schiffer, Q. Huang, R. J. Cava, J. W. Lynn, and M. Hasan, Spin order by quantum frustration in triangular lattice Mott insulator $NaCrO_2$: A neutron scattering study, arXiv:1405.6184.

[67] T. Moriya, Nuclear Magnetic Relaxation in Antiferromagnetics, Prog. Theor. Exp. Phys. **16**, 23 (1956).

[68] D. Beeman and P. Pincus, Nuclear Spin-Lattice Relaxation in Magnetic Insulators, Phys. Rev. **166**, 359 (1968).

[69] M. Majumder, M. Prinz-Zwick, S. Reschke, A. Zubtsovskii, T. Dey, F. Freund, N. Büttgen, A. Jesche, I. Kézsmárki, A. A. Tsirlin, and P. Gegenwart, Field evolution of low-energy excitations in the hyperhoneycomb magnet $\beta$-Li$_2$IrO$_3$, Phys. Rev. B **101**, 214417 (2020).

[70] G. E. Pake, *Paramagnetic resonance: an introductory monograph*, Vol. 1 (WA Benjamin, New York, 1962).

[71] S. Angelov, J. Darriet, C. Delmas, and G. L. Flem, Relation between the EPR linewidths and the exchange integrals in $A$CrO$_2$ ($A=$ Li, Na, and K), Solid State Commun. **50**, 345 (1984).

[72] R. Kubo and K. Tomita, A general theory of magnetic resonance absorption, J. Phys. Soc. Jpn. **9**, 888 (1954).

[73] A. Zorko, *Determination of Magnetic Anisotropy by EPR in Topics* edited by A. M. Maghraby (IntechOpen, London, 2019).

[74] A. Zorko, M. Pregelj, A. Potočnik, J. van Tol, A. Ozarowski, V. Simonet, P. Lejay, S. Petit, and R. Ballou, Role of Antisymmetric Exchange in Selecting Magnetic Chirality in Ba$_3$NbFe$_3$Si$_2$O$_{14}$, Phys. Rev. Lett. **107**, 257203 (2011)

[1] The dipolar coupling constant at the H site is calculated using lattice sum with an assumption of $1\mu_B$ magnetic moment on each Cr$^{3+}$ ion to be $\sim$ 0.150 kOe/$\mu_B$ per Cr$^{3+}$ ion.

[2] Note that the ratio of the NMR and $\mu$ SR relaxation rates $(1/T_1)_{NMR}/(1/T_1)_{\mu SR}$ scales with the ratio of the coupling constants squared. An order of magnitude can be calculated from the ratio of $\mu$SR internal field found at 1.5 K and the product of the hyperfine constant by the Cr$^{3+}$ moment, assumed to be $3.87\mu_B$ or accordingly from the 5 kG HWHM of the NMR spectrum at 1.5 K. At 15 K, this yields a rough estimate of $(T_1)_{NMR}$, of the order of 9-25 $\mu$s, which explains well the wipe-out.

[3] Note that the difference in the extension of this regime can be due in the way extrapolations of transverse relaxation $T_2$ plots have been performed which is always fairly delicate when $T_2$ is short.